Facile Synthesis with TiO$_2$ Xerogel and Urea Enhanced Aniline Aerofloat Degradation Performance of Direct Z-Scheme Heterojunction TiO$_2$/g-C$_3$N$_4$ Composite

Sipin Zhu [1,2], Zhiyong Chen [3], Chunying Wang [1,2], Jiahao Pan [1,2] and Xianping Luo [1,2,*]

[1] Faculty of Resource and Environmental Engineering, Jiangxi University of Science and Technology, Ganzhou 341000, China; zhusipin926@163.com (S.Z.); beyond_life@163.com (C.W.); thekid123go@163.com (J.P.)
[2] Jiangxi Key Laboratory of Mining & Metallurgy Environmental Pollution Control, Ganzhou 341000, China
[3] Ganfeng Lithium Co., Ltd., Ganzhou 341000, China; 18970142740@163.com
[*] Correspondence: luoxianping9491@163.com; Tel.: +86-135-0797-9491

Abstract: Different TiO$_2$/g-C$_3$N$_4$ (TCN) composites were synthesized by a simple pyrolysis method with TiO$_2$ xerogel and urea. The structure and physicochemical properties of TCN were characterized by X-ray diffraction, scanning electron microscope, transmission electron microscope, ultraviolet-visible diffuse reflectance spectrum, X-ray photoelectron spectroscopy, N$_2$-adsorption isotherms and electrochemical impedance spectroscopy. Aniline Aerofloat was chosen as a typical degradation-resistant contaminant to investigate the photodegradation activity of TCN under UV irradiation. The results indicated that TCN had higher light absorption intensity, larger specific surface area and smaller particle size compared to pure TiO$_2$. Furthermore, TCN had great recycling photocatalytic stability for the photodegradation of Aniline Aerofloat. The photocatalytic activity depends on the synergistic reaction between holes (h$^+$) and hydroxyl radicals (·OH). Meanwhile, the direct Z-scheme heterojunction structure of TiO$_2$ and g-C$_3$N$_4$ postpones the recombination of h$^+$ and electrons to enhance UV-light photocatalytic activity.

Keywords: titanium dioxide; graphite phase carbon nitride; photocatalysis; Aniline Aerofloat

1. Introduction

Aniline Aerofloat (dianilinodithiophosphoric acid, AAF, (C$_6$H$_5$NH)$_2$PSSH) has been used frequently as an efficient flotation collecting agent for lead-zinc sulfide ore in China [1]. It was discharged with flotation wastewater into nature although it is highly toxic and contains dithiophosphate and aniline groups [2–4]. Moreover, AAF has been hard to degrade thoroughly so far. Some degradation methods have been researched such as sodium hypochlorite oxidation [5], vacuum ultraviolet/ozone [6], chelate precipitation [7], and so on. Thereinto, photocatalytic degradation has great potential to degrade AAF quickly, easily, and effectively.

In the photocatalytic degradation of organic pollution, titanium dioxide (TiO$_2$) has been researched extensively in dyes, endocrine disrupters, pesticides, etc., as a photocatalyst [8–10]. It deserves more attention even as a commercialized attribute to safety, non-toxicity, stability, high-performance, and low cost [11–13]. However, TiO$_2$ was limited in practical applications due to its wide bandgap (3.2 eV) and the rapid recombination of electron (e$^-$) and hole (h$^+$). The construction of TiO$_2$/semiconductor heterojunction is an effective method in many ways. Graphene carbon nitride (g-C$_3$N$_4$) has a narrow bandgap (2.7 eV) with an electronic structure, excellent visible light responding and is easy to prepare in the meantime [14,15]. Therefore, g-C$_3$N$_4$ was identified as an appropriate and complementary semiconductor to composite TiO$_2$/semiconductor heterojunction [16–18]. For example, Tan et al. prepared Ti^{3+} self-doped TiO$_2$/g-C$_3$N$_4$ heterojunctions via solid-state

chemical reduction, and the material showed better degradation of phenol and production of hydrogen [19]. Wei et al. synthesized mesoporous brookite/anatase TiO_2/g-C_3N_4 heterojunction hollow microspheres that had a more negative conduction band and a wider light absorption range [20]. Mesoporous TiO_2/g-C_3N_4 composite was fabricated by Zhang et al. had about 50 times the removal rate of enrofloxacin than pure g-C_3N_4, which attribute to the O–Ti–N bond interface heterojunction between TiO_2 and g-C_3N_4 separated and transferred charge carriers efficiently [21]. To enhance TiO_2 light response, a uniform mesopore TiO_2/g-C_3N_4 composite with core/shell heterojunction structure was prepared by Xia et al., and the uniform mesoporous g-C_3N_4 nanosheets were used to decorate TiO_2 spheres [22].

The TiO_2/g-C_3N_4 composite was studied deeply by lots of specialists and multitudinous synthesis methods and raw materials were exploited. In the synthesis process of TiO_2/g-C_3N_4, there are many ways to prepare such as adding g-C_3N_4 powder in a precursor solution of TiO_2, depositing $TiCl_4$ precursor onto the surface of the g-C_3N_4 powder, mixing TiO_2 powder with melamine in solution, and so on [23–26].

To our knowledge, even though so many methods were adopted to prepare TiO_2/g-C_3N_4 composite, TiO_2 xerogel has not been directly mixed with urea as raw materials to synthesize the composite. TiO_2 xerogel was used rather than commercial TiO_2 (P25), which could compose better with g-C_3N_4 during TiO_2 catalyst forming. In this work, TiO_2/g-C_3N_4 composite was synthesized by simple pyrolysis with urea and TiO_2 xerogel, and AAF was selected as the potential pollutant to detect the photocatalytic activities of the prepared composite catalyst. Synthesis conditions including the mass ratio of TiO_2 to C_3N_4, calcination temperature, calcination time, and heating rate were studied detailed. X-ray diffraction, scanning electron microscope, transmission electron microscope, ultraviolet-visible diffuse reflectance spectrum, X-ray photoelectron spectroscopy N_2-adsorption isotherms and electrochemical impedance spectroscopy were all characterized to analyze the heterojunction structure and physicochemical properties of TiO_2/g-C_3N_4. Furthermore, the stability and mechanism of TiO_2/g-C_3N_4 were also deduced.

2. Materials and Methods

2.1. Materials

Aniline Aerofloat (AAF, $(C_6H_5NH)_2PSSH$, 99.5%): Hunan Mingzhu Flotation Reagents Limited Company, Hunan, China. Ethylene glycol (CH_3CH_2OH, 99.7%): Tianjin Guangfu Science and Technology Development Co., Ltd., Tianjin, China. Glacial acetic acid (CH_3COOH, 99.5%): Xilong Scientific Co., Ltd., Guangdong, China. Ammonium oxalate ($(NH_4)C_2O_4$, 99.8%): Damao Chemical Reagent Factory, Tianjin, China. Methanol (CH_3OH, 99.9%), tetrabutyl titanate ($Ti(OC_4H_9)_4$, 98.0%), isopropanol (C_3H_8O, 99.7%) and urea ($(NH_2)_2CO$, 99.0%): Sinopharm Chemical Reagent Co., Ltd., Shanghai, China. The reagents above are all used without further purification.

2.2. Synthesis of Photocatalysts

2.2.1. Synthesis of TiO_2 Xerogel

The TiO_2 xerogel was prepared by the sol-gel method [27,28]. In preparing solutions A and B, respectively, solution A was the mixture consisting of 10 mL ethyl alcohol and 2 mL glacial acetic acid; solution B could be obtained when the 10 mL tetrabutyl titanate was dripped into 15 mL ethyl alcohol slowly at a speed of $0.1 \ mL·s^{-1}$ with magnetic stirring. The next step is adding solution A to solution B at a speed of $0.1 \ mL·s^{-1}$, the transparent colloid was obtained after 30 min. The transparent colloid was naturally aged for 48 h and dried in the oven at 90 °C for 24 h. Finally, xerogel powder was collected after ground.

2.2.2. Synthesis of TiO_2/g-C_3N_4

According to previous reports [29–32], TiO_2/g-C_3N_4 composite photocatalysts were prepared with a simple pyrolysis process. Urea (20 g) and TiO_2 xerogel powder (2, 1, 0.67, 0.5, 0.4 g) were mixed and vibrated for 30 min with ultrasonic (KQ5200E, 40 KHz, Kunshan Ultrasonic Instruments Co., Ltd., Kunshan, China). The solid mixture was placed into

the ceramic crucible with a cover and calcined at different temperatures for several hours at a heating rate with the muffle furnace. The details are illustrated in Scheme 1. The resultant powder which was ground and collected after cooling to an ambient temperature was TiO_2/g-C_3N_4 composite denoted as TCN. TiO_2/g-C_3N_4 composite with a doping mass ratio of x and a heating rate of 5 °C·min^{-1}, 550 °C for 6 h is denoted as TCN-U$_x$. TiO_2/g-C_3N_4 composite with a doping mass ratio of 20 and a heating rate of 10 °C·min^{-1}, y °C for 6 h is denoted as TCN-T$_y$. TiO_2/g-C_3N_4 composite with a doping mass ratio of 20 and a heating rate of z °C·min^{-1}, 550 °C for 6 h is denoted as TCN-R$_z$. TiO_2/g-C_3N_4 composite with a doping mass ratio of 20 and a heating rate of 10 °C·min^{-1}, 550 °C for n h is denoted as TCN-H$_n$ (x = m_{urea}·$m_{xerogel}^{-1}$ = 10, 20, 30, 40, 50; y = 450, 500, 550, 600, 650; z = 5, 10, 15, 20, 25; n = 2, 3, 4, 5, 6, 7).
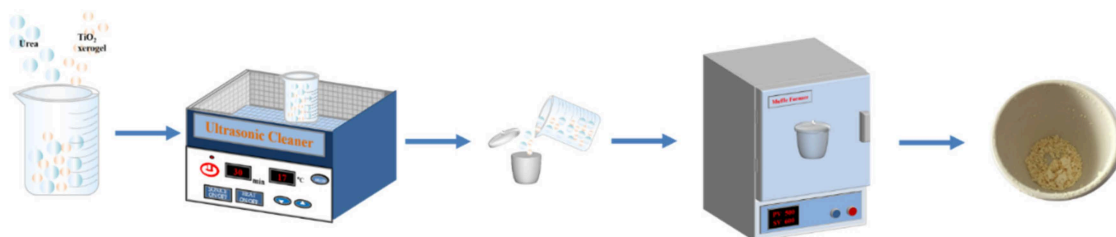
Scheme 1. The synthesis of simple TiO_2/g-C_3N_4 by pyrolysis process.

2.3. Characterization

X'TRA rotating anode powder X-ray diffraction (XRD, PANalytical B.V., X'Pert powder) with Cu Kα radiation (λ = 0.154056 nm) in the diffraction angle range of 2θ = 10~90° with 0.02° interval. The sample's phase and composition were identified by it. The morphology of TCN was exhibited by scanning electron microscope (FE SEM, Tescan, Brno, Czech Republic, MIRA3 LMH). Crystal and element imaging of samples were shown via transmission electron microscope (TEM, FEI, Tecnai Hillsboro, USA, G2-20) connected with a CCD camera from Gatan Company (Pleasanton, CA, USA) and X-ray energy dispersive spectrometer from EDAX Company. Ultraviolet-visible diffuse reflectance spectrum (UV-Vis DRS, Shimadzu, Kyoto, Japan, UV-2600PC) was employed in the range of 200~800 nm with 1 nm interval to obtain the optical absorption spectra of materials, and $BaSO_4$ was used as the reference. The Brunauer–Emmett–Teller (BET) surface area and Barrett–Joyner–Halenda (BJH) pore width were analyzed by Micromeritics ASAP 2460 nitrogen adsorption apparatus. X-ray photoelectron spectroscopy (XPS, Thermo, Waltham, MA, USA, ESCALAB 250Xi) spectra were operated with a monochromatic Al Kα radiation source (1486.6 eV) and the binding energies were adjusted with C1s (284.8 eV). Electrochemical impedance spectroscopy (EIS) was analyzed by three-electrode cell electrochemical workstation (CHI-660E, Chinstruments, Shanghai, China) with Pt and saturated calomel electrode as the counter and reference electrode, and 0.1 mol·L^{-1} Na_2SO_4 aqueous solution as electrolyte. The sample (10 mg) was dispersed in 1 mL ethylalcohol with ultrasonic for 30 min, and then the mixture was dispersed uniformly on the indium tin oxide (ITO) glass as a working electrode within a 1.0 cm^2 area.

2.4. Photocatalytic Degradation and Analysis

The photocatalytic activity of TCN was explored by degradation of AAF under ultraviolet light provided by a 300 W mercury lamp. All photocatalysis experiments were implemented with the rotary photochemical reaction instrument (XPA-7, Xujiang Electromechanical Plant, Nanjing, China). The catalyst of TCN (30 mg) was dispersed in the AAF solution (50 mL, 100 mg·L^{-1}) contained in the quartz tube. The first 30 min of the reaction were in the dark to reach absorption equilibrium, and then they were illuminated for 180 min. After every given time interval, 5 mL of solution was obtained and filtered through a 0.45 μm water filtration membrane to be analyzed by high-performance liquid chromatography (HPLC, 1260 infinity, Agilent, Santa Clara, CA, USA).

The concentration of AAF was tested by HPLC, equipped with eclipse plus C18 (3.5 μm, 4.6 mm × 150 mm) and the temperature of the chromatograph column was 30 °C, The measured wavelength was set as 230 nm according to the full wavelength scanning by ultraviolet-visible spectrophotometer (T6 New century, Beijing Persee General Co., Ltd., Beijing, China). The mobile phase consists of water and methanol (v/v = 60:40) and flows at 1 mL·min^{-1}. The degradation efficiency was calculated by C_t/C_0, in which C_0 and C_t were the concentration of AAF at the beginning and a certain time.

At the same time, the catalyst was reused 4 times under the same conditions to investigate the stability and the prospects for practicality in industrial. Reactive active species hole (h^+) and hydroxyl radical ($\cdot$OH) in the photocatalytic degradation process were analyzed by quenching agent ammonium oxalate and isopropanol experiments.

3. Results and Discussion

3.1. Morphology Analysis

SEM images of pure TiO_2, g-C_3N_4, TCN-U_{20} and TCN-T_y shown in Figures 1a–c and S1 provided that TiO_2 and g-C_3N_4 were composed successfully. As we can see, the TCN composite combined with the structure of the lamellae g-C_3N_4 stack on bulk TiO_2. The thickness and density of g-C_3N_4 lamellae increase, respectively, which made the poriness and active positions more with the doping ratio and calcination temperature higher. Nevertheless, overmuch g-C_3N_4 lamellae would impede UV-light absorption of TiO_2 which was covered and thus weaken the photocatalytic activity of CNT. Meanwhile, the TEM image of TCN-U_{20} shown in Figure 1d suggested the lattice spaces of 0.350 nm and 0.320 nm correspond to the plane (101) of TiO_2 and the plane (002) of the g-C_3N_4 [33,34]. The results of mapping images and EDS spectrum in Figure 1e showed the percent of C, N, O and Ti. The atom percent of C and N is approximately 0.73~0.89 conforming to 0.75 that the ratio of C and N in g-C_3N_4. Because of the oxygen in the air, the atom percent of Ti and O is approximately 0.30~0.31, which is far less than 0.5 that the ratio of Ti and O in TiO_2. The results suggested doping of g-C_3N_4 is successful and the formation of the heterojunction between TiO_2 and g-C_3N_4.
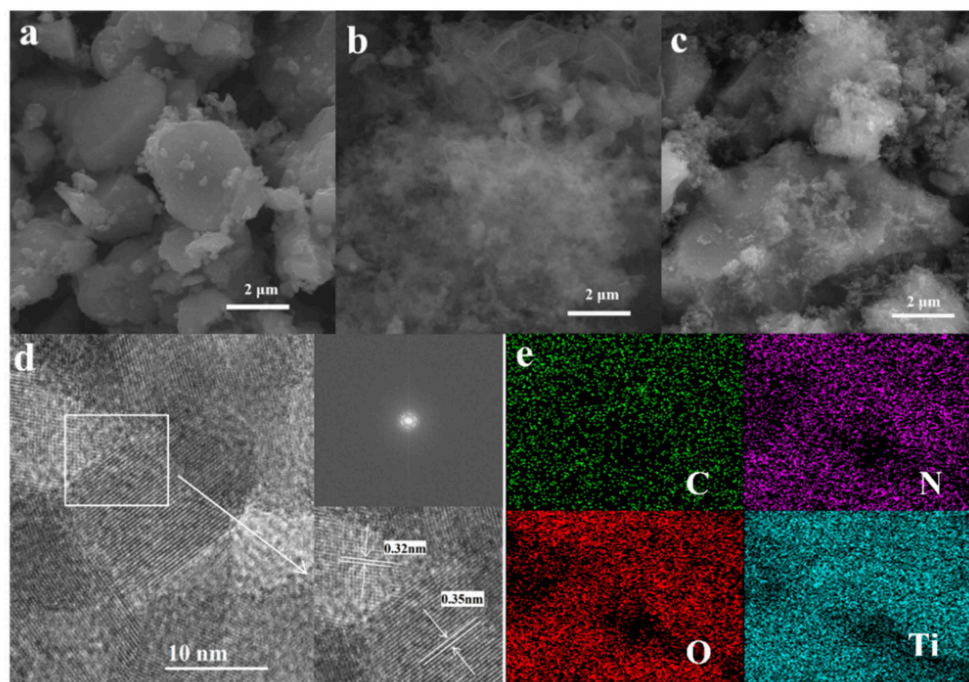
Figure 1. SEM images of (**a**) pure TiO_2, (**b**) g-C_3N_4, and (**c**) TCN-U_{20}; (**d**) TEM image, (**e**) mapping images of TCN-U_{20}.

3.2. XRD Analysis

The crystal phases of TCN, pure g-C_3N_4 and TiO_2 are exhibited in Figures 2a and S2. Diffraction peaks at 25.3°, 37.8° and 48.0° were pointed to (101), (004) and (200) of anatase TiO_2 (JCPDS 21-1272). Peaks at 27.4°, 36.1°, 41.2° and 54.3° are pointed to (110), (101), (111) and (211) of rutile TiO_2 (JCPDS 21-1276), and peaks at 12.9° and 27.7° correspond to (100) in the in-plane repetitive unit of tri-s-triazine and (002) attributed to interlayer stacking of g-C_3N_4 (JCPDS 87-1526) [35–37]. Almost all TCN samples were mixed with the rutile phase and anatase phase of TiO_2. Observing all XRD patterns of TCN, it is indistinguishable if the peak at 27.7° belongs to the phase of g-C_3N_4 due to low loading and overlapped peaks [38]. The calculated crystalline phase ratio and cell parameters of TCN are shown in Tables 1 and S1. The growth of the TiO_2 rutile phase was suppressed with the doping of g-C_3N_4, and the ratio was lowest when the doping ratio was 20. Similarly, the other results can be seen in Table S1. The growth of the TiO_2 rutile phase was also suppressed with the heating rate, and the ratio was lowest when the heating rate was 10, and the growths of the TiO_2 rutile phase were both always promoted with the temperature and heat preservation hour. Suggesting the changes of diffraction peaks were caused by the transformation between TiO_2 anatase and rutile and the growth of crystal particles. Excellent mixed ratios of TiO_2 anatase and rutile when the weight percent of the anatase phase was 76.8 or 73.8 and the rutile phase was 23.2 or 26.2 demonstrated excellent photocatalytic activity [39,40]. The change in lattice size was caused by the formation of a heterojunction between g-C_3N_4 and TiO_2 [33]. Obviously, the crystal phase ratio of TiO_2 anatase and rutile changed with TCN preparation conditions. To clear the relationship between TCN degradation efficiency of AAF and the ratio of TiO_2 anatase, the degradation efficiency plots were fitted with a curve as shown in Figure 2b. The fittted curve was obtained by the power function with six and the correlation coefficient R-square is 0.618. So, the change of crystal phase ratio not only decided cell size but also affected the photocatalytic activity significantly [41].
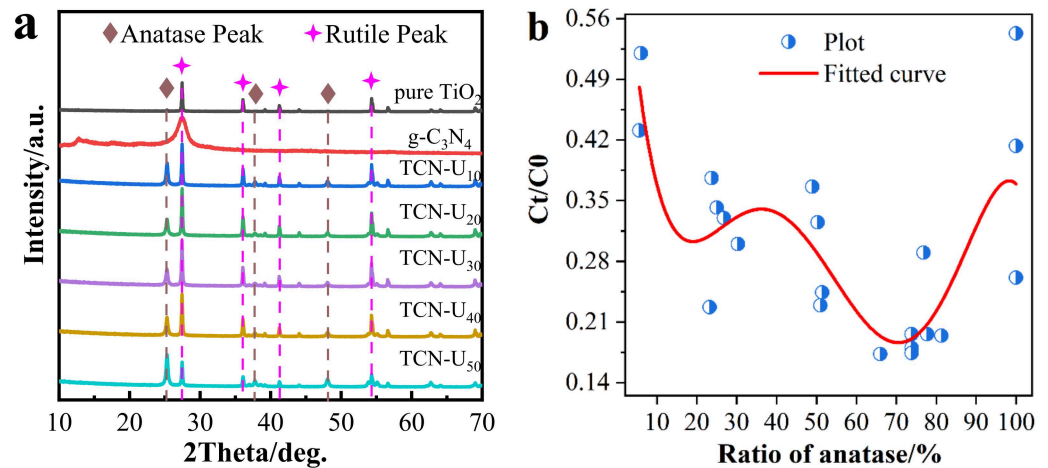
Figure 2. (**a**) XRD patterns of pure TiO_2, g-C_3N_4 and TCN-U_x and (**b**) fitted curve between photocatalytic degradation efficiency of AAF and ratio of TiO_2 anatase.

Table 1. Crystalline phase ratio and cell parameters of pure TiO_2 and TCN-U_x.

Sample	Anatase/wt%	Rutile/wt%	*a = b*/nm	*c*/nm
Pure TiO_2	5.6	94.4	1.42442	2.08097
10:1	30.3	69.7	1.30545	1.99599
20:1	76.8	23.2	0.80742	1.74158
30:1	23.7	76.3	1.05978	2.33788
40:1	26.8	73.2	1.19316	2.29493
50:1	48.9	51.1	1.10269	2.11718

3.3. UV-Vis DRS Analysis

The ultraviolet light absorption intensity of all TCN samples was much stronger than pure g-C$_3$N$_4$ and TiO$_2$ as shown in Figures 3a and S3a–c suggested the doped of g-C$_3$N$_4$ enhanced the UV-light absorption intensity significantly. Furthermore, the bandgap was calculated by the Kubelka–Munk function Equation (1) as follows:

$$\alpha h\nu = A\left(h\nu - E_g\right)^2 \tag{1}$$

where α, h, ν, A, and E_g was absorption coefficient, Planck constant, light frequency, a constant, and optical bandgap energy, respectively. The bandgap calculation spectra shown in Figures 3b and S3d–f and the results indicated that different preparation conditions influenced the bandgaps to different degrees. Combined with the XRD results, it can be inferred that the change in UV-light absorption intensity and bandgap were related to the formation of the TiO$_2$/g-C$_3$N$_4$ heterojunction and TiO$_2$ phase transformation between anatase and rutile [42–44].
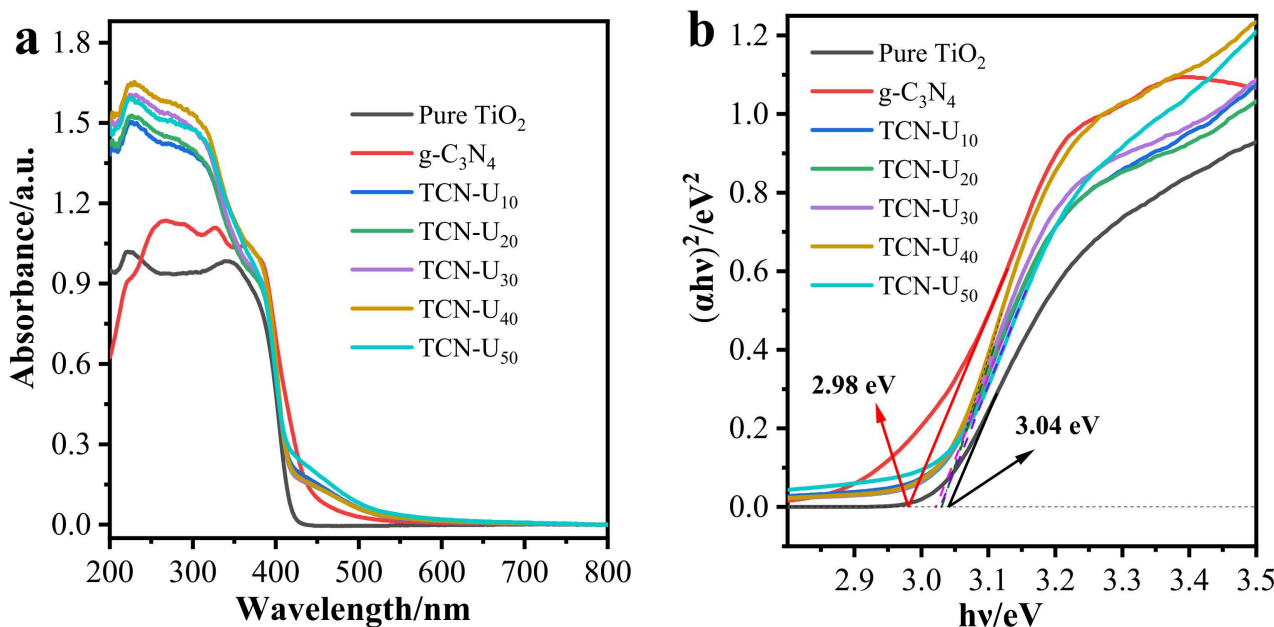
Figure 3. UV-Vis DRS spectra (**a**) and bandgap calculation spectra (**b**) of pure TiO$_2$, g-C$_3$N$_4$ and TCN-U$_x$.

3.4. S_{BET} and Porosity Analysis

N$_2$ adsorption-desorption isotherms and pore size distribution of TCN-U$_x$ and pure TiO$_2$ showed in Figure 4. The BET fitted curve and specific surface area data of TCN-U$_x$ are exhibited in Figure S4, Tables 2 and S2. Compared with pure TiO$_2$, S_{BET} of TCN increased 3–7 times after g-C$_3$N$_4$ doping. All samples showed the typical IV isotherm with H1 hysteresis loops reflecting the existence of homogeneous mesoporous. The hysteresis loops were caused by capillary condensation in the relative pressure (P/P$_0$) range of about 0.5–1.0. The results suggested that TCN has a bigger specific surface area and smaller pore size than pure TiO$_2$. TCN performed high photocatalytic activity demonstrated by a bigger specific surface area, more abundant mesoporous structure, and more adsorption sites [39]. The increase of S_{BET} was attributed to covered g-C$_3$N$_4$ increased with doping ratio, and growth of TiO$_2$ anatase with heating rate sped within range of 10 °C/min. The decrease of SBET was due to the growth of TiO$_2$ rutile with a heating rate speed from 10 to 25 °C/min, calcination temperature raised from 450 to 650 °C, and heating preservation hour increasing from 2 to 7 h. The results were consistent with the XRD and SEM characterization of the samples.
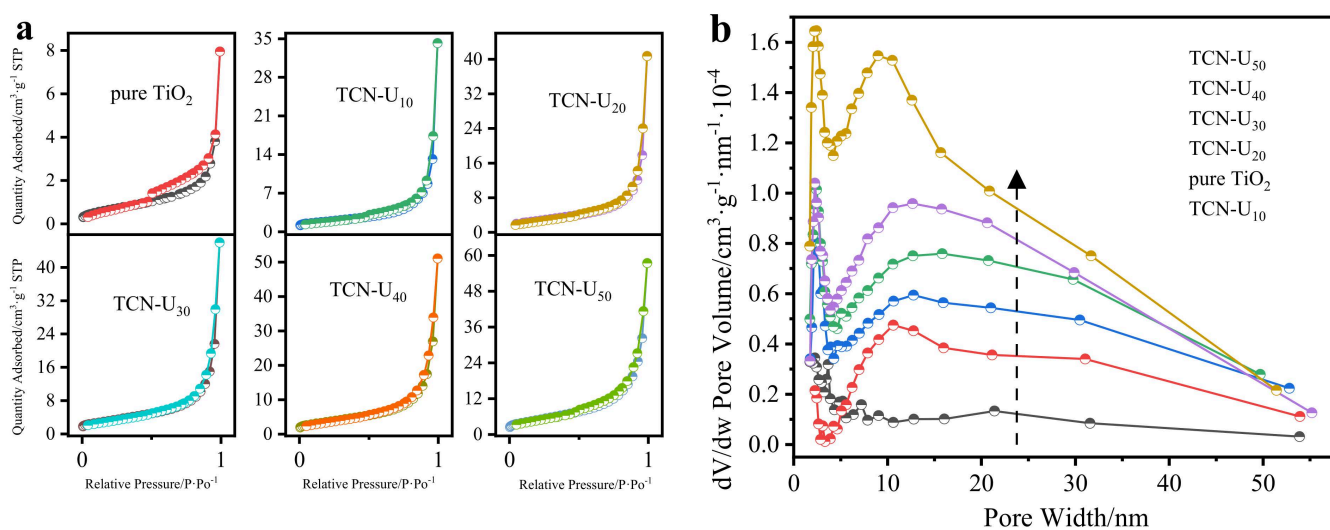
Figure 4. N$_2$ adsorption-desorption isotherms (**a**) and pore size distribution (**b**) of pure TiO$_2$, g-C$_3$N$_4$ and TCN-U$_x$.

Table 2. Specific surface area of pure TiO$_2$ and U$_x$T$_{550}$R$_5$H$_6$-TCN.

Sample	g-C$_3$N$_4$	Pure TiO$_2$	10:1	20:1	30:1	40:1	50:1
Surface area(m^2·g^{-1})	121.0	2.5	7.3	9.7	11.7	13.1	18.1

3.5. Photodegradation Experiment

The photocatalytic degradation of AAF by TCN (Figure 5) was always higher than by commercial TiO$_2$ (P25) and pure TiO$_2$ prepared, which might be attributed to the formation of the TiO$_2$/g-C$_3$N$_4$ heterojunction [29,44–47]. The TCN samples with a 20 doping ratio, 10 °C·min^{-1}, 550 °C, 6 h in the same three other conditions showed the optimum photocatalytic degradation efficiency.

The performance of photocatalytic degradation could be attributed to these reasons as results of characterization showed: the bigger specific surface area and more active positions with the doping ratio of g-C$_3$N$_4$ compared with pure TiO$_2$, transforming from urea to g-C$_3$N$_4$ smoother with the heating rate, completeness, and crystallinity of TiO$_2$/g-C$_3$N$_4$ composite better with the calcination temperature and heating preservation hour. However, the excessive g-C$_3$N$_4$ would obstruct the UV-light absorption to TiO$_2$ with the further increase of doping ratio. The transformation process was too fast to attach uniformly to the TiO$_2$ surface resulting in stacking, and TCN got heavily agglomerated with the further rise in calcination temperature. Moreover, a suitable ratio of TiO$_2$ rutile phases and anatase phases is a vital contribution to promoting photocatalytic degradation efficiency [40,41,48]. On the whole, the calcination temperature has the greatest influence on the photocatalytic activity of aniline aerofloat degradation, followed by the doping ratio, heat preservation hour and heating rate have the least influence in a certain range.

The stability of the photocatalyst is an important index to estimate the photocatalytic activity so it is significant to study the recycling of the TiO$_2$/g-C$_3$N$_4$ composite. At room temperature, TCN-T$_{550}$ (30 mg) was added to a 50 mL AAF solution (100 mg·L^{-1}). The catalyst used was collected and reused in the next degradation experiment. The results of reusing catalyst photocatalytic activity were showed in Figure 6. After four times of recycling, the TiO$_2$/g-C$_3$N$_4$ composite photocatalytic degradation efficiency of AAF was always steadily high, indicating that the TiO$_2$/g-C$_3$N$_4$ composite is a kind of potential photocatalyst for practical engineering application.
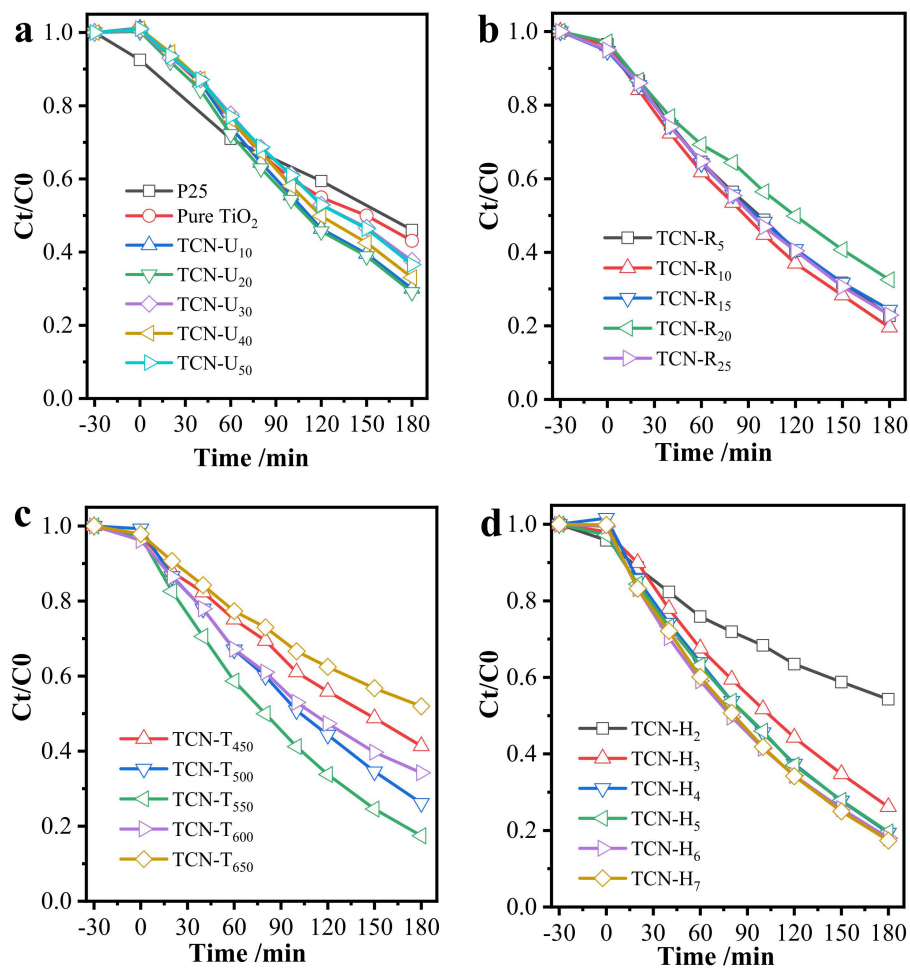
Figure 5. Activity of (**a**) TCN-U$_x$, (**b**) TCN-R$_z$, (**c**) TCN-T$_y$, (**d**) TCN-H$_n$ on the photocatalytic degradation of AAF.
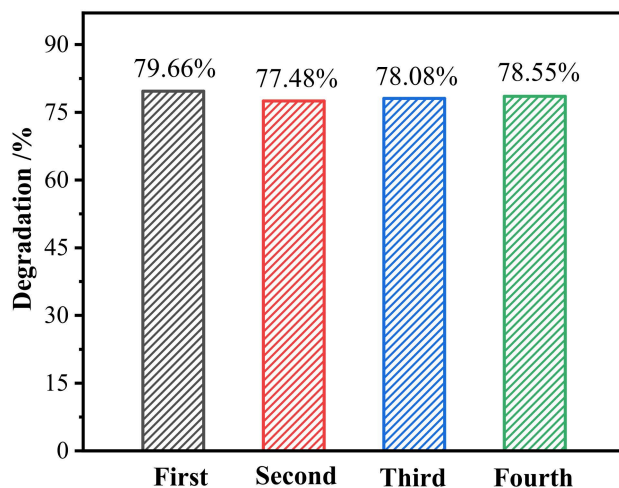
Figure 6. Activity of recycling test of TCN-T$_{550}$ for photocatalytic degradation of AAF.

3.6. XPS Analysis

The surface chemical compositions of TCN-T$_{550}$ were tested by XPS and the results shown in Figure 7 show survey, C1s, N1s, O1s and Ti2p scans. The peaks at 284.6 eV, 285.3 eV, and 288.6 eV shown in Figure 7b correspond to the sp^2 C–C, C=, N–C=N bonds [49]. Meanwhile, the binding energies of 399.3 eV and 400.6 eV shown in Figure 7c

correspond to the sp^3 N-(C)$_3$ and interstitial N, which indicated the existence of g-C$_3$N$_4$ and composite structure [8,50]. Binding energies in 529.8 eV and 530.6 eV shown in Figure 7d corresponds to Ti–O band and surface absorbed –OH [44], and binding energies in 458.6 eV and 464.3 eV shown in Figure 7e were attributed to Ti 2p$_{3/2}$ and Ti 2p$_{1/2}$ [51], which directly testified TiO$_2$. Furthermore, there no peaks of C–O, N–O, Ti–C, or Ti–N observed indicating that TiO$_2$ and g-C$_3$N$_4$ were composed with molecule doping rather than lattice replace.
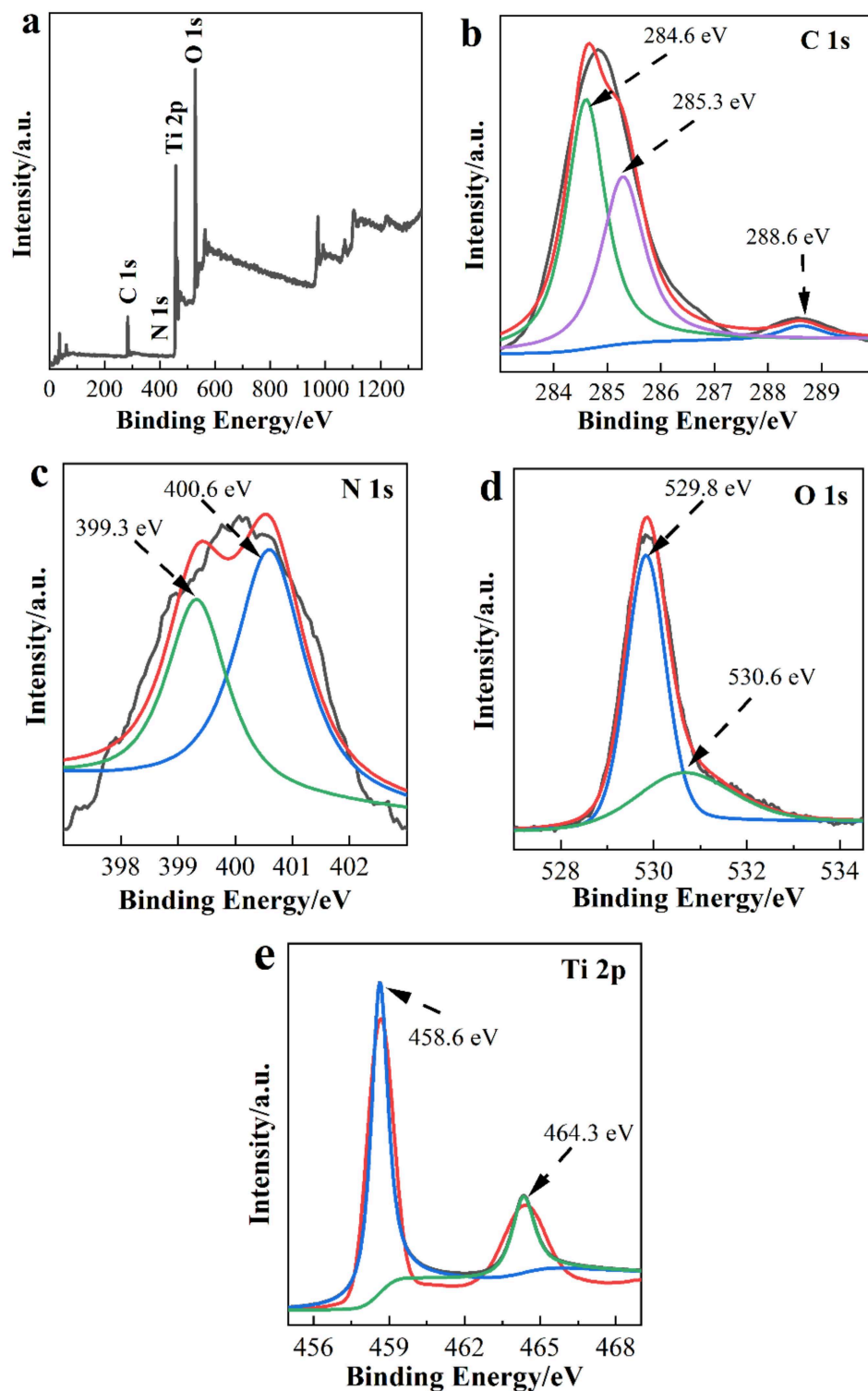
Figure 7. XPS of survey (**a**), C1s (**b**), N1s (**c**), O1s (**d**) and Ti2p (**e**) scans of TCN-T$_{550}$.

3.7. Electrochemical Analysis

The electrochemical impedance spectroscopy (EIS) of pure TiO_2 and TCN-T$_{550}$ shown in Figure 8 indicated that e^--h^+ pair separation-effective of TCN-T$_{550}$ is more efficient than TiO_2 [49].
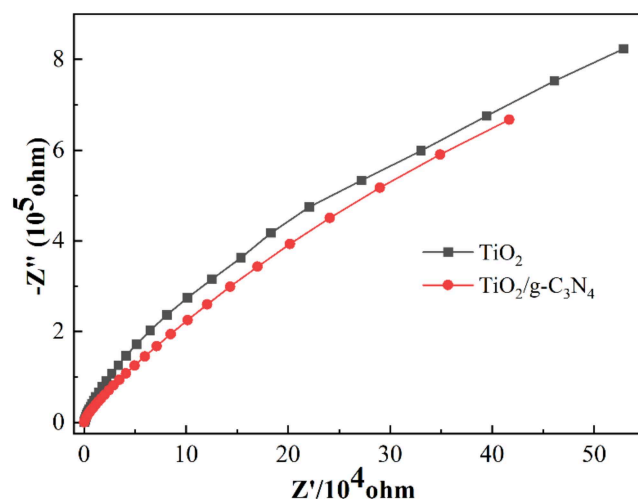
Figure 8. The EIS of pure TiO_2 and TCN-T$_{550}$.

3.8. Mechanism of Composite

3.8.1. Reactive Active Species of Photocatalyst

Research of photocatalysts' reactive active species in the photocatalytic degradation process is the fundamental research of photocatalytic mechanism. As we all know, ammonium oxalate is the quenching agent of hole (h^+), and isopropanol is the quenching agent of hydroxyl radical (·OH). The results are shown in Figure 9.
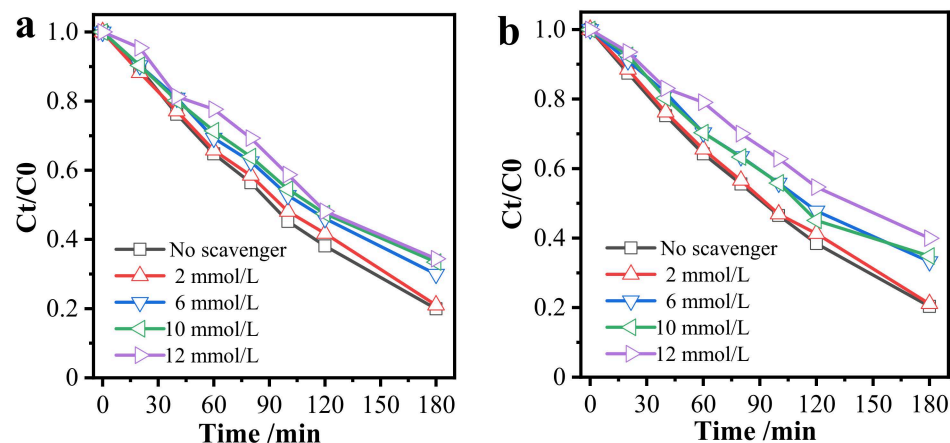
Figure 9. Effect of TCN-T$_{550}$ for photocatalytic of AAF degradation with different concentration quenching agents: (**a**) ammonium oxalate, (**b**) isopropanol.

The photocatalytic degradation of AAF efficiency declined gradually with the increasing concentration of ammonium oxalate and isopropanol shown in Figure 9. The result illustrates the oxidation action of h^+ and ·OH in the photocatalytic degradation process. Meanwhile, the effect of ammonium oxalate and isopropanol on the photocatalytic degradation efficiency is similarly judged from the degradation efficiency decrement. In conclusion, the h^+ and ·OH, which were both photocatalysts reactive active species in the photocatalytic degradation process, react synergistically in the photocatalytic reaction system.

3.8.2. Mechanism Conjecture of Photodegradation

The bandgap energy of TiO_2 and $g-C_3N_4$ were 3.04 eV and 2.98 eV, which is based on UV-Vis DRS results. The valence band (VB) and conduction band (CB) edge potentials were calculated by the following Equations (2) and (3) [52]:

$$E_{VB} = \chi - E^e + \frac{1}{2}E_g \tag{2}$$

$$E_{CB} = E_{VB} - E_g \tag{3}$$

where E_{VB}, E_{CB}, χ, E^e and E_g were the VB edge potential, the CB edge potential, the geometric mean of Mulliken electronegativity [53], and the energy of electrons on the hydrogen scale (~4.5 eV, vs. NHE) and optical bandgap energy. The value of χ of TiO_2 and $g-C_3N_4$ were 5.81 eV [54] and 4.73 eV [55]. The E_{VB} of TiO_2 and $g-C_3N_4$ were 2.83 eV and 1.72 eV, and the E_{CB} of TiO_2 and $g-C_3N_4$ were calculated as –0.21 eV and −1.26 eV, respectively. The VB potential of TiO_2 (2.83 eV) is more positive than $H_2O/\cdot OH$ (+1.99 eV vs. NHE), and the CB potential of $g-C_3N_4$ is more negative than $O_2/\cdot O_2^-$ (-0.33 eV vs. NHE) [56], so there was an oxidation reaction in the VB of TiO_2 and reduction reaction in the CB of $g-C_3N_4$. This result and the results of photocatalysts reactive active species confirmed each other. TiO_2 and $g-C_3N_4$ might form type-II or direct Z-scheme heterojunction. If it belongs to type-II heterojunction, e^- on the CB of $g-C_3N_4$ would transfer to the CB of TiO_2 and h^+ on the VB of TiO_2 would transfer to the VB of $g-C_3N_4$. However, the VB potential of $g-C_3N_4$ (1.72 eV) is more negative than $H_2O/\cdot OH$ (+1.99 eV vs. NHE) and cannot produce $\cdot OH$ which was the active species. The conclusion is contradictory to the result of the quenching experiment. So, the possible photodegradation mechanism process was conjectured as a direct Z-scheme heterojunction shown in Figure 10 [57] and following Equations (4)–(8):

$$TiO_2/g-C_3N_4 + h\nu \rightarrow TiO_2\ (e^-, h^+)/g-C_3N_4\ (e^-, h^+) \tag{4}$$

$$TiO_2\ (e^-, h^+)/g-C_3N_4\ (e^-, h^+) \rightarrow TiO_2\ (h^+) + g-C_3N_4\ (e^-) \tag{5}$$

$$TiO_2\ (h^+) + H_2O \rightarrow \cdot OH + H\cdot \tag{6}$$

$$g-C_3N_4\ (e^-) + O_2 \rightarrow \cdot O_2^- \tag{7}$$

$$\cdot OH/TiO_2\ (h^+)/\cdot O_2^- + Aniline\ Aerofloat \rightarrow products \tag{8}$$
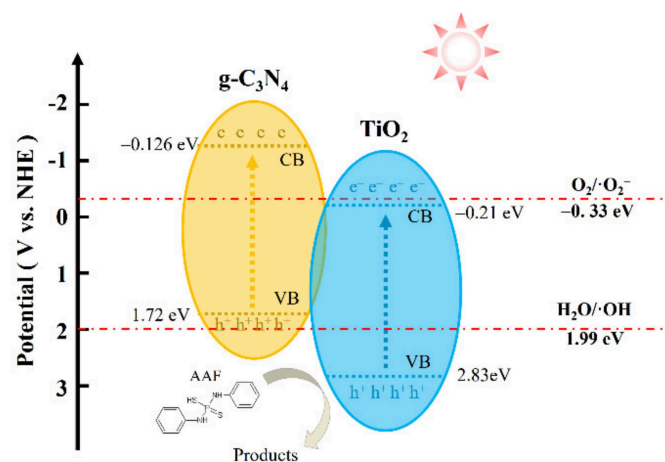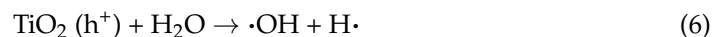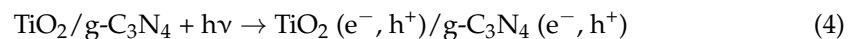
Figure 10. The possible photodegradation mechanism process of $TiO_2/g-C_3N_4$.

Under light irradiation excitation, e^- in transfers from CB to VB of TiO_2 and $g-C_3N_4$ severally, and there is h^+ left in CB. Meanwhile, e^- of TiO_2 combines with h^+ of $g-C_3N_4$ on the VB of $g-C_3N_4$. Next h^+ of TiO_2 oxidizes the H_2O molecule into $\cdot OH$ and $H\cdot$ and

e^- of g-C_3N_4 reduces the O_2 molecule into $\cdot O_2^-$. Then, $\cdot OH$, h^+ and $\cdot O_2^-$, which all have oxidizability, can oxidize the Aniline Aerofloat molecule into degraded products.

4. Conclusions

TiO$_2$/g-C$_3$N$_4$ composites with different doping ratios, heating rates, calcination temperatures and heating preservation hours were synthesized successfully by a simple pyrolysis method with the raw material of TiO$_2$ xerogel and urea. TCN samples with a 20 doping ratio, 10 °C·min^{-1}, 550 °C, 6 h in the same three other conditions showed the optimum photocatalytic degradation efficiency. The excellent activity was attributed to the appropriate crystal phase ratio of TiO$_2$ rutile phases and anatase phases, high UV-light absorption intensity, big specific surface area, and formation of the TiO$_2$/g-C$_3$N$_4$ heterojunction. In addition, the TiO$_2$/g-C$_3$N$_4$ heterojunction could postpone the recombination of h^+ and e^- to extend the reaction time and enhance the photodegradation efficiency. Furthermore, TiO$_2$/g-C$_3$N$_4$ composites have great photodegradation stability for AAF after four times.

References

1. He, M.F. Research on Key Technology in the Beneficiation of Sn-Bearing Refractory Lead-zine Mine in Southeast Yunnan. Ph.D. Thesis, Central South University, Changsha, China, 2012.
2. Xiang, L.; Xiao, T.; Mo, C.-H.; Zhao, H.M.; Li, Y.W.; Li, H.; Cai, Q.Y.; Zhou, D.M.; Wong, M.H. Sorption kinetics, isotherms, and mechanism of aniline aerofloat to agricultural soils with various physicochemical properties. *Ecotoxicol. Environ. Saf.* **2018**, *154*, 84–91. [CrossRef] [PubMed]
3. Fu, P.; Ma, Y.; Lei, B.; Li, G.; Lin, X. Decomposition of refractory aniline aerofloat collector in aqueous solution by an ozone/vacuum-UV (O$_3$/VUV) process. *Environ. Technol.* **2021**, *42*, 659–670. [CrossRef] [PubMed]
4. Fu, P.; Wang, L.; Li, G.; Hou, Z.; Ma, Y. Homogenous catalytic ozonation of aniline aerofloat collector by coexisted transition metallic ions in flotation wastewaters. *J. Environ. Chem. Eng.* **2020**, *8*, 103714. [CrossRef]
5. Lin, W.; Tian, J.; Ren, J.; Xu, P.T.; Dai, Y.K.; Sun, S.Y.; Wu, C. Oxidation of aniline aerofloat in flotation wastewater by sodium hypochlorite solution. *Environ. Sci. Pollut. Res.* **2016**, *23*, 785–792. [CrossRef]
6. Deng, X.; Zhang, D.; Wu, M.; Antwi, P.; Su, H.; Lai, C. Enhanced removal of refractory pollutant from aniline aerofloat wastewater using combined vacuum ultraviolet and ozone (VUV/O$_3$) process. *Water Sci. Technol.* **2019**, *80*, 2250–2259. [CrossRef]
7. Jie, X.; Wang, H.; Chen, Y. Removal of dianiline dithiophosphoric acid from wastewater by chelate precipitation. *Desalin. Water Treat.* **2016**, *57*, 5100–5107. [CrossRef]

8. Liu, H.; Yu, D.; Sun, T.; Du, H.; Jiang, W.; Muhammad, Y.; Huang, L. Fabrication of surface alkalinized g-C$_3$N$_4$ and TiO$_2$ composite for the synergistic adsorption-photocatalytic degradation of methylene blue. *Appl. Surf. Sci.* **2019**, *473*, 855–863. [CrossRef]

9. Rashid, J.; Abbas, A.; Chang, L.C.; Iqbal, A.; Haq, I.U.; Rehman, A.; Awan, S.U.; Arshad, M.; Rafique, M.; Barakat, M.A. Butterfly cluster like lamellar BiOBr/TiO$_2$ nanocomposite for enhanced sunlight photocatalytic mineralization of aqueous ciprofloxacin. *Sci. Total Environ.* **2019**, *665*, 668–677. [CrossRef]

10. Pang, N.N.; Lin, H.F.; Hu, J.Y. Photodegradation of fluazaindolizine in aqueous solution with graphitic carbon nitride nanosheets under simulated sunlight illumination. *Ecotoxicol. Environ. Saf.* **2019**, *170*, 33–38. [CrossRef]

11. Zheng, X.; Liu, Y.; Liu, X.; Li, Q.; Zheng, Y. A novel PVDF-TiO$_2$@g-C$_3$N$_4$ composite electrospun fiber for efficient photocatalytic degradation of tetracycline under visible light irradiation. *Ecotoxicol. Environ. Saf.* **2021**, *210*, 111866. [CrossRef]

12. Balu, S.; Chen, Y.-L.; Yang, T.C.K.; Chen, J.-N.; Chen, S.-W. Effect of ultrasound-induced hydroxylation and exfoliation on P90-TiO$_2$/g-C$_3$N$_4$ hybrids with enhanced optoelectronic properties for visible-light photocatalysis and electrochemical sensing. *Ceram. Int.* **2020**, *46*, 18002–18018. [CrossRef]

13. Wu, Z.; Liang, Y.; Yuan, X.; Zou, D.; Fang, J.; Jiang, L.; Zhang, J.; Yang, H.; Xiao, Z. MXene Ti$_3$C$_2$ derived Z-scheme photocatalyst of graphene layers anchored TiO$_2$/g-C$_3$N$_4$ for visible light photocatalytic degradation of refractory organic pollutants. *Chem. Eng. J.* **2020**, *394*, 124921. [CrossRef]

14. Du, X.; Bai, X.; Xu, L.; Yang, L.; Jin, P. Visible-light activation of persulfate by TiO$_2$/g-C$_3$N$_4$ photocatalyst toward efficient degradation of micropollutants. *Chem. Eng. J.* **2020**, *384*, 123245. [CrossRef]

15. Zhang, Y.; Xu, J.; Mei, J.; Sarina, S.; Wu, Z.; Liao, T.; Yan, C.; Sun, Z. Strongly interfacial-coupled 2D-2D TiO$_2$/g-C$_3$N$_4$ heterostructure for enhanced visible-light induced synthesis and conversion. *J. Hazard. Mater.* **2020**, *394*, 122529. [CrossRef]

16. Wang, J.; Ma, J.; Zhang, Q.; Chen, Y.; Hong, L.; Wang, B.; Chen, J.; Jing, H. New heterojunctions of CN/TiO$_2$ with different band structure as highly efficient catalysts for artificial photosynthesis. *Appl. Catal. B Environ.* **2021**, *285*, 119781. [CrossRef]

17. Zhou, P.; Shen, Y.; Zhao, S.; Li, G.; Cui, B.; Wei, D.; Shen, Y. Synthesis of clinoptilolite-supported BiOCl/TiO$_2$ heterojunction nanocomposites with highly-enhanced photocatalytic activity for the complete degradation of xanthates under visible light. *Chem. Eng. J.* **2021**, *407*, 126697. [CrossRef]

18. Iqbal, A.; Kafizas, A.; Sotelo-Vazquez, C.; Wilson, R.; Ling, M.; Taylor, A.; Blackman, C.; Bevan, K.; Parkin, I.; Quesada-Cabrera, R. Charge Transport Phenomena in Heterojunction Photocatalysts: The WO$_3$/TiO$_2$ System as an Archetypical Model. *ACS Appl. Mater. Interfaces* **2021**, *13*, 9781–9793. [CrossRef]

19. Xiu, Z.; Xing, Z.; Li, Z.; Wu, X.; Yan, X.; Hu, M.; Cao, Y.; Yang, S.; Zhou, W. Ti^{3+}-TiO$_2$/Ce^{3+}-CeO$_2$ Nanosheet heterojunctions as efficient visible-light-driven photocatalysts. *Mater. Res. Bull.* **2018**, *100*, 191–197. [CrossRef]

20. Wei, H.; McMaster, W.A.; Tan, J.Z.Y.; Chen, D.; Caruso, R.A. Tricomponent brookite/anatase TiO$_2$/g-C$_3$N$_4$ heterojunction in mesoporous hollow microspheres for enhanced visible-light photocatalysis. *J. Mater. Chem. A* **2018**, *6*, 7236–7245. [CrossRef]

21. Zhang, R.; Yu, Y.; Wang, H.; Du, J. Mesoporous TiO$_2$/g-C$_3$N$_4$ composites with O-Ti-N bridge for improved visible-light photodegradation of enrofloxacin. *Sci. Total Environ.* **2020**, *724*, 138280. [CrossRef]

22. Xia, Y.; Xu, L.; Peng, J.; Han, J.; Guo, S.; Zhang, L.; Han, Z.; Komarneni, S. TiO$_2$@g-C$_3$N$_4$ core/shell spheres with uniform mesoporous structures for high performance visible-light photocatalytic application. *Ceram. Int.* **2019**, *45*, 18844–18851. [CrossRef]

23. Zi, T.-Q.; Zhao, X.-R.; Liu, C.; Cao, Y.-Q.; Li, A.-D. A facile route to prepare TiO$_2$/g-C$_3$N$_4$ nanocomposite photocatalysts by atomic layer deposition. *J. Alloy. Compd.* **2021**, *855*, 157446. [CrossRef]

24. Sun, S.; Ding, H.; Mei, L.; Chen, Y.; Hao, Q.; Chen, W.; Xu, Z.; Chen, D. Construction of SiO2-TiO$_2$/g-C$_3$N$_4$ composite photocatalyst for hydrogen production and pollutant degradation: Insight into the effect of SiO$_2$. *Chin. Chem. Lett.* **2020**, *31*, 2287–2294. [CrossRef]

25. Song, J.; Huang, M.; Jiang, N.; Zheng, S.; Mu, T.; Meng, L.; Liu, Y.; Liu, J.; Chen, G. Ultrasensitive detection of amoxicillin by TiO$_2$-g-C$_3$N$_4$@AuNPs impedimetric aptasensor: Fabrication, optimization, and mechanism. *J. Hazard. Mater.* **2020**, *391*, 122024. [CrossRef]

26. Meng, Z.; Zhou, B.; Xu, J.; Li, Y.; Hu, X.; Tian, H. Heterostructured Nitrogen and Sulfur Co-doped Black TiO$_2$/g-C$_3$N$_4$Photocatalyst with Enhanced Photocatalytic Activity. *Chem. Res. Chin. Univ.* **2020**, *36*, 1045–1052. [CrossRef]

27. Zhu, S.P.; Wang, C.Y.; Luo, X.P. Preparation and degradation activity for benzohydroxamic acid of Gd-doped anatase TiO$_2$ photocatalysts. *J. Chin. Ceram. Soc.* **2017**, *45*, 1523–1530. [CrossRef]

28. Zhu, S.P.; Wang, C.Y.; Wei, Z.Y.; Chen, Z.Y.; Wu, C.T.; Luo, X.P. Degradation activity for aniline aerofloat of Sm-doped TiO$_2$ photocatalysts. *J. Chin. Ceram. Soc.* **2018**, *46*, 1632–1638. [CrossRef]

29. Tan, Y.G.; Shu, Z.; Zhou, J.; Li, T.; Wang, W.; Zhao, Z. One-step synthesis of nanostructured g-C$_3$N$_4$/TiO$_2$ composite for highly enhanced visible-light photocatalytic H$_2$ evolution. *Appl. Catal. B Environ.* **2018**, *230*, 260–268. [CrossRef]

30. Niu, P.; Zhang, L.L.; Liu, G.; Cheng, H.M. Graphene-Like Carbon Nitride Nanosheets for Improved Photocatalytic Activities. *Adv. Funct. Mater.* **2012**, *22*, 4763–4770. [CrossRef]

31. Tripathi, A.; Narayanan, S. Impact of TiO$_2$ and TiO$_2$/g-C$_3$N$_4$ Nanocomposite to Treat Industrial Wastewater. *Environ. Nanotechnol. Monit. Manag.* **2018**, *10*, 280–291. [CrossRef]

32. Yousefzadeh, S. Effect of thermal condensation temperature on electrochemical capacitive properties of g-C$_3$N$_4$ supported on reduced TiO$_2$ nanowires/nanotubes array. *J. Alloy. Compd.* **2019**, *785*, 1–6. [CrossRef]

33. Pan, J.; You, M.; Chi, C.; Dong, Z.; Wang, B.; Zhu, M.; Zhao, W.; Song, C.; Zheng, Y.; Li, C. The two dimension carbon quantum dots modified porous g-C_3N_4/TiO_2 nano-heterojunctions for visible light hydrogen production enhancement. *Int. J. Hydrogen Energy* **2018**, *43*, 6586–6593. [CrossRef]

34. Pan, J.; Dong, Z.; Wang, B.; Jiang, Z.Y.; Zhao, C.; Wang, J.J.; Song, C.S.; Zheng, Y.Y.; Li, C.R. The enhancement of photocatalytic hydrogen production via Ti^{3+} self-doping black TiO_2/g-C_3N_4 hollow core-shell nano-heterojunction. *Appl. Catal. B Environ.* **2019**, *242*, 92–99. [CrossRef]

35. Zhu, H.; Yang, X.; Zhang, M.; Li, Q.; Yang, J. Construction of 2D/2D TiO_2/g-C_3N_4 nanosheet heterostructures with improved photocatalytic activity. *Mater. Res. Bull.* **2020**, *125*, 110765. [CrossRef]

36. Zhang, H.; Liu, Z.; Li, Y.; Zhang, C.; Wang, Y.; Zhang, W.; Wang, L.; Niu, L.; Wang, P.; Wang, C. Intimately coupled TiO_2/g-C_3N_4 photocatalysts and in-situ cultivated biofilms enhanced nitrate reduction in water. *Appl. Surf. Sci.* **2020**, *503*, 144092. [CrossRef]

37. Zada, A.; Khan, M.; Qureshi, M.N.; Liu, S.-Y.; Wang, R. Accelerating Photocatalytic Hydrogen Production and Pollutant Degradation by Functionalizing g-C_3N_4 With SnO_2. *Front. Chem.* **2020**, *7*, 941. [CrossRef]

38. Du, L.; Jin, C.; Cheng, Y.; Xu, L.; An, X.; Shang, W.; Zhang, Y.; Rao, X. Improvement of antibacterial activity of hydrothermal treated TC_4 substrate through an in-situ grown TiO_2/g-C_3N_4 Z-scheme heterojunction film. *J. Alloy. Compd.* **2020**, *842*, 155612. [CrossRef]

39. Sun, Q.; Hu, X.L.; Zheng, S.L.; Zhang, J.; Sheng, J.W. Effect of calcination on structure and photocatalytic property of N-TiO_2/g-C_3N_4@diatomite hybrid photocatalyst for improving reduction of Cr(VI). *Environ. Pollut.* **2019**, *245*, 53–62. [CrossRef]

40. Wang, W.K.; Chen, J.J.; Zhang, X.; Huang, Y.X.; Li, W.W.; Yu, H.Q. Self-induced synthesis of phase-junction TiO_2 with a tailored rutile to anatase ratio below phase transition temperature. *Sci. Rep.* **2016**, *6*, 20491. [CrossRef]

41. Wang, X.L.; Li, C. Roles of Phase Junction in Photocatalysis and Photoelectrocatalysis. *J. Phys. Chem. C* **2018**, *122*, 21083–21096. [CrossRef]

42. Lei, J.; Chen, B.; Lv, W.; Zhou, L.; Wang, L.; Liu, Y.; Zhang, J. An inverse opal TiO_2/g-C_3N_4 composite with a heterojunction for enhanced visible light-driven photocatalytic activity. *Dalton Trans.* **2019**, *48*, 3486–3495. [CrossRef]

43. Fang, Y.; Huang, W.; Yang, S.; Zhou, X.; Ge, C.; Gao, Q.; Fang, Y.; Zhang, S. Facile synthesis of anatase/rutile TiO_2/g-C_3N_4 multi-heterostructure for efficient photocatalytic overall water splitting. *Int. J. Hydrogen Energy* **2020**, *45*, 17378–17387. [CrossRef]

44. Li, G.; Wu, Y.; Zhang, M.; Chu, B.; Huang, W.; Fan, M.; Dong, L.; Li, B. Enhanced Removal of Toxic Cr(VI) in Wastewater by Synthetic TiO_2/g-C_3N_4 Microspheres/rGO Photocatalyst under Irradiation of Visible Light. *Ind. Eng. Chem. Res.* **2019**, *58*, 8979–8989. [CrossRef]

45. Lin, X.; Sun, M.; Gao, B.; Ding, W.; Zhang, Z.; Anandan, S.; Umar, A. Hydrothermally regulating phase composition of TiO2 nanocrystals toward high photocatalytic activity. *J. Alloy. Compd.* **2021**, *850*, 156653. [CrossRef]

46. Zhu, Y.; Liu, Y.; Ai, Q.; Gao, G.; Yuan, L.; Fang, Q.; Tian, X.; Zhang, X.; Egap, E.; Ajayan, P.M.; et al. In Situ Synthesis of Lead-Free Halide Perovskite–COF Nanocomposites as Photocatalysts for Photoinduced Polymerization in Both Organic and Aqueous Phases. *ACS Mater. Lett.* **2022**, *4*, 464–471. [CrossRef]

47. Kipkorir, A.; Dubose, J.; Cho, J.; Kamat, P.V. $CsPbBr_3$–CdS heterostructure: Stabilizing perovskite nanocrystals for photocatalysis. *Chem. Sci.* **2021**, *12*, 14815–14825. [CrossRef]

48. Colomer, M.T.; Campo, A.D. Preparation of nanostructured TiO_2 films with high catalytic activity and their 3D spatial distribution of anatase and rutile phases. *J. Mater. Sci.* **2019**, *54*, 9414–9425. [CrossRef]

49. Jin, C.; Li, Z.; Zhang, Y.; Wang, M.; Wu, Z.; Xie, Y.; Wang, Y.; Zhu, T. The construction of g-C_3N_4/Sm^{2+} doped Bi_2WO_6 2D/2D Z-scheme heterojunction for improved visible-light excited photocatalytic efficiency. *Sep. Purif. Technol.* **2019**, *224*, 33–43. [CrossRef]

50. Li, J.; Li, B.; Li, Q.; Yang, J. The effect of N-doped form on visible light photoactivity of Z-scheme g-C_3N_4/TiO_2 photocatalyst. *Appl. Surf. Sci.* **2019**, *466*, 268–273. [CrossRef]

51. Li, C.; Lou, Z.; Yang, Y.; Wang, Y.; Lu, Y.; Ye, Z.; Zhu, L. Hollowsphere Nanoheterojunction of g-C_3N_4@TiO_2 with High Visible Light Photocatalytic Property. *Langmuir* **2019**, *35*, 779–786. [CrossRef]

52. Nethercot, A. Prediction of Fermi Energies and Photoelectric Thresholds Based on Electronegativity Concepts. *Phys. Rev. Lett.* **1974**, *33*, 1088–1091. [CrossRef]

53. Mulliken, R.S. A New Electroaffinity Scale; Together with Data on Valence States and on Valence Ionization Potentials and Electron Affinities. *J. Chem. Phys.* **1934**, *2*, 782–793. [CrossRef]

54. Corpus-Mendoza, A.N.; Moreno-Romero, P.M.; Hu, H. Evaluation of Mulliken Electronegativity on $CH_3NH_3PbI_3$ Hybrid Perovskite as a Thought-Provoking Activity. *J. Chem. Educ.* **2019**, *96*, 974–978. [CrossRef]

55. Hao, R.; Wang, G.; Tang, H.; Sun, L.; Xu, C.; Han, D. Template-free preparation of macro/mesoporous g-C_3N_4/TiO_2 heterojunction photocatalysts with enhanced visible light photocatalytic activity. *Appl. Catal. B Environ.* **2016**, *187*, 47–58. [CrossRef]

56. Liu, Y.; Zeng, X.; Hu, X.; Hu, J.; Zhang, X. Two-dimensional nanomaterials for photocatalytic water disinfection: Recent progress and future challenges. *J. Chem. Technol. Biotechnol.* **2019**, *94*, 22–37. [CrossRef]

57. Zhu, B.C. Research on Adsorption and Photocatalytic Activity of g-C_3N_4: First-Principle Calculation and Experimental Study. Ph.D. Thesis, Wuhan University of Technology, Wuhan, China, 2018.